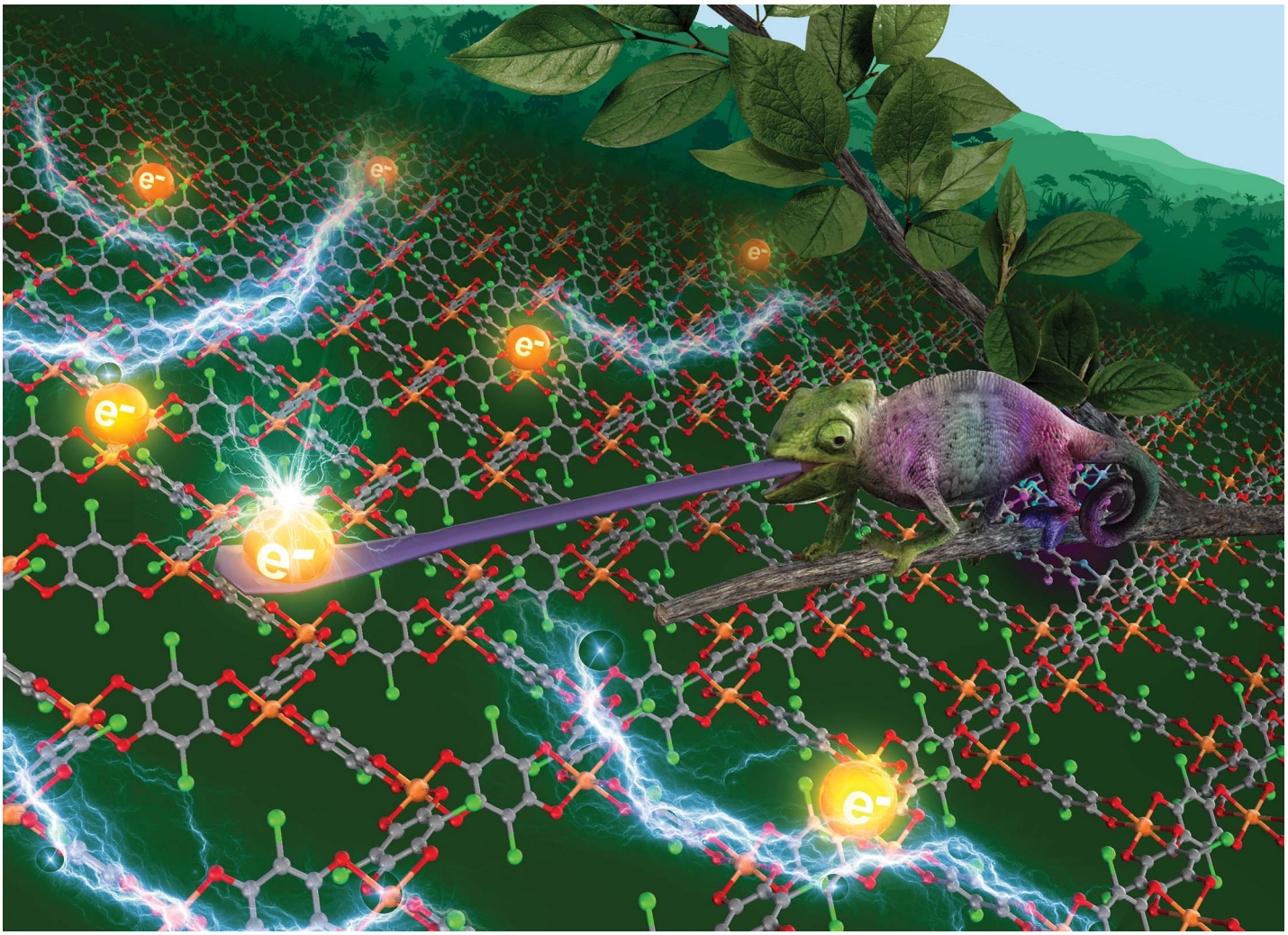

Showcasing research from Professor Miyasaka's laboratory, Institute for Materials Research, Tohoku University, Sendai, Japan.

Chameleonic layered metal–organic frameworks with variable charge-ordered states triggered by temperature and guest molecules

This paper presents a two-dimensional honeycomb layer compound composed of tetraoxolene-bridged iron subunits whose charge-ordered state is multiply variable in five states involving intra-lattice electron transfers triggered by thermal treatments and solvation/desolvation. The compound is $(NPr_4)_2[Fe_2(Cl_2An)_3]$ (NPr_4^+ = tetra-*n*-propylammonium; Cl_2An^{2-} = 2,5-dichloro-3,6-dihydroxo-1,4-benzoquinonate). This type of material could be a candidate for multiple-switching systems accessible by various kinds of external stimuli.

As featured in:

See Hitoshi Miyasaka *et al.*, *Chem. Sci.*, 2020, **11**, 3610.

ROYAL SOCIETY OF CHEMISTRY

rsc.li/chemical-science

Registered charity number: 207890

Chemical Science

ROYAL SOCIETY OF CHEMISTRY

EDGE ARTICLE

View Article Online
View Journal | View Issue

Cite this: *Chem. Sci.*, 2020, **11**, 3610

All publication charges for this article have been paid for by the Royal Society of Chemistry

Chameleonic layered metal–organic frameworks with variable charge-ordered states triggered by temperature and guest molecules†

Jian Chen,[ab] Yoshihiro Sekine,[ab] Atsushi Okazawa,[c] Hiroyasu Sato,[d] Wataru Kosaka[ab] and Hitoshi Miyasaka *[ab]

Received 5th February 2020
Accepted 4th March 2020

DOI: 10.1039/d0sc00684j

rsc.li/chemical-science

Molecular materials whose electronic states are multiply varied depending on external stimuli are among the most promising targets for the development of multiply accessible molecular switches. Here, we report a honeycomb layer composed of tetraoxolene-bridged iron (Fe) subunits whose charge-ordered states are multiply variable *via* thermal treatments and solvation/desolvation with the crystallinity intact. The compound is $(NPr_4)_2[Fe_2(Cl_2An)_3]$ (**1-d**; NPr_4^+ = tetra-*n*-propylammonium; Cl_2An^{2-} = 2,5-dichloro-3,6-dihydroxo-1,4-benzoquinonate), which possesses three charge-ordered states: a low-temperature (LT) phase $[(Fe^{3+})_2(Cl_2An^{2-})(Cl_2An^{\bullet 3-})_2]^{2-}$; an intermediate (IM) phase $[(Fe^{2.5+})_2(Cl_2An^{2-})(Cl_2An^{2.5-})_2]^{2-}$; and a high-temperature (HT) phase $[(Fe^{2+})_2(Cl_2An^{2-})_3]^{2-}$ that varies according to temperature. In addition, the LT phase of **1-d** is reversibly changeable to another IM phase in its solvated compound **1** *via* a solvation/desolvation process at room temperature. This example demonstrates a new multiple-switching system based on electron transfer and host–guest chemistry in a charge-flexible metal–organic framework.

Introduction

Stimuli-responsive molecular materials (SRMMs), which change their phases according to applied external stimuli, have good potential for use as near-future molecular scale devices such as high-density molecular memories, molecular switches, or sensors.[1–3] One of the most intriguing targets for SRMMs is a class of thermally driven electron transfer (TDET) systems,[1–31] which can also be a strong candidate for SRMMs triggered by other external stimuli such as light,[12,14,16,19,20,23,32–35] pressure,[6,36] and chemical guests.[26,37–39] Therefore, to date, various types of TDETs, such as neutral–ionic transition (N–I transition),[5,9,18,25,27,38] valence tautomerism (VT),[4,6,8,10,11,21,22,24,28,30,31] and inter-valence electron transfer (IVET),[7,13] have been investigated using organic charge-transfer systems and metal complexes. Most of these systems have been studied using a one-step TDET that occurs at one transition temperature $T_{1/2(1)}$, and only a few examples of two- or multi-step TDET with $T_{1/2(1)}$, $T_{1/2(2)}$, and $T_{1/2(x)}$ ($T_{1/2(1)} < T_{1/2(2)} < T_{1/2(x)}$) have been reported thus far: (i) discrete molecules, where two VT subunits interact electronically with each other, *i.e.*, owing to electronic disproportionation,[10,21,22] (ii) discrete molecules with intermediate states composed of several alternately arranged species possessing different charge-ordered states produced by stepwise IVET, which may be affected by Coulomb interactions and/or elastic interactions,[15,16,29] and (iii) N–I transition chains with inter-chain Coulomb interactions.[18,25,27] In addition, there is another case (iv), where two crystallographically independent VT subunits, each of which undergoes VT at a different temperature, are present in one system.[17,28]

Considering such TDET systems that possess electronic disproportionation states, two-dimensional (2D) layered systems with a formula of D_xA_y ($x \neq y$) may be good candidates (Fig. 1). Recently, we have reported one-step TDET in a D_2A_3-type honeycomb-layered compound, $(NPr_4)_2[Fe_2(Cl_2An)_3]\cdot 2(acetone)\cdot H_2O$ (**1**), which is composed of 2,5-dichloro-3,6-dihydroxo-1,4-benzoquinonate (Cl_2An^{m-}) and Fe^{n+} ions with tetrapropylammonium cations (NPr_4^+) as well as some crystallization solvents (acetone and water) located at hexagonal pores of layers and between layers.[31] This layered compound revealed two ground states of the fully electron transferred state (as the low-temperature (LT) phase) of $[(Fe^{3+})_2(Cl_2An^{2-})(Cl_2An^{\bullet 3-})_2]^{2-}$ and a charge-disproportionate ordered state (defined as the charge-ordered intermediate (IM_o) phase) of $[(Fe^{2+})(Fe^{3+})(Cl_2An^{2-})_2(Cl_2An^{\bullet 3-})]^{2-}$ with a boundary at $T_{1/2a}\uparrow$ =

[a]*Institute for Materials Research, Tohoku University, 2-1-1 Katahira, Aoba-ku, Sendai 980-8577, Japan. E-mail: miyasaka@imr.tohoku.ac.jp*

[b]*Department of Chemistry, Graduate School of Science, Tohoku University, 6-3 Aramaki-Aza-Aoba, Aoba-ku, Sendai 980-8578, Japan*

[c]*Department of Basic Science, Graduate School of Arts and Sciences, The University of Tokyo, 3-8-1 Komaba, Meguro-ku, Tokyo 153-8902, Japan*

[d]*Application Laboratory, Rigaku Corporation, 3-9-12, Matsubara-cho, Akishima-shi, Tokyo 196-8666, Japan*

† Electronic supplementary information (ESI) available. CCDC 1971740–1971743. For ESI and crystallographic data in CIF or other electronic format see DOI: 10.1039/d0sc00684j

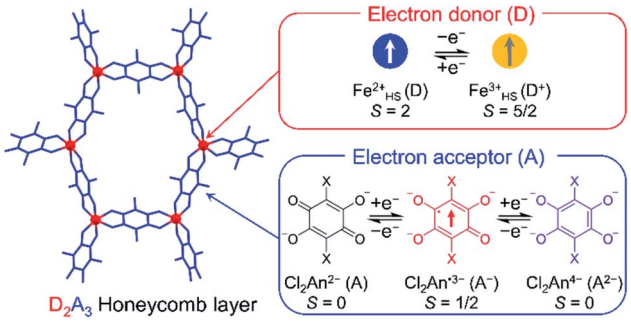

Fig. 1 Structure of D_2A_3-type honeycomb-layered systems constructed from an Fe^{2+} center (D in red) and Cl_2An^{2-} (A in blue), where the Fe^{2+} center acts as the electron donor (D) to be Fe^{3+} (D^+), whereas Cl_2An^{2-} acts as the electron donor (A) and may be reduced to be $Cl_2An^{\bullet 3-}$ (A^-).

237 K ($T_{1/2a}\downarrow$ = 236 K, where the signs ↑ and ↓ refer to heating and cooling processes, respectively. Moreover, $T_{1/2a}$ is $T_{1/2(1)}$ for **1**). The Cl_2An^{m-} bridging ligand can take three redox-active states of $\underline{Cl_2An^{2-}} + e^- \rightarrow \underline{Cl_2An^{\bullet 3-}}$ and $Cl_2An^{\bullet 3-} + e^- \rightarrow \underline{Cl_2An^{4-}}$ and *vice versa*, whereas Fe^{n+} takes $Fe^{2+} \rightarrow Fe^{3+} + e^-$ and *vice versa* in this type of material (Fig. 1). Thus, the LT phase is a layer that is constructed from D^+A^- chains bridged by Cl_2An^{2-} (L_B), where D^+ and A^- are high-spin Fe^{3+} and $Cl_2An^{\bullet 3-}$ (L_A), respectively, while the IM_o phase is a layer where DA chains and D^+A^- chains are alternately aligned with the Cl_2An^{2-} (L_B) bridges (Scheme 1). In other words, this D_2A_3 layer system can be assumed to be a layered DA chain as a sort of one-dimensional (1D) VT system.[30]

This feature of charge-ordered states made us imagine the existence of a neutral state of the high-temperature (HT) phase in **1**, which comprises only DA chains at higher temperatures; practically, **1** converted itself to a solvent-free form, $(NPr_4)_2[Fe_2(Cl_2An)_3]$ (**1-d**), with an elimination of its lattice solvents, and no longer changes to the HT phase within **1** upon heating. Nevertheless, **1-d** afforded three TDET phases (LT → IM → HT) described in Scheme 1 with two-step TDET at $T_{1/2b}$ and $T_{1/2c}$ appearing continuously from the IM_o phase of **1** *via* desolvation ($T_{1/2b}$ and $T_{1/2c}$ are $T_{1/2(1)}$ and $T_{1/2(2)}$ for **1-d**, respectively) (Scheme 2). In addition, the conversion between **1-d** and **1** is reversible *via* a solvation/desolvation treatment.

Here, we report the first example of multi-step TDET in a layered D_2A_3 compound (**1-d**), which is continuously linked to another TDET-form (**1**) involving a guest-induced ET in a single

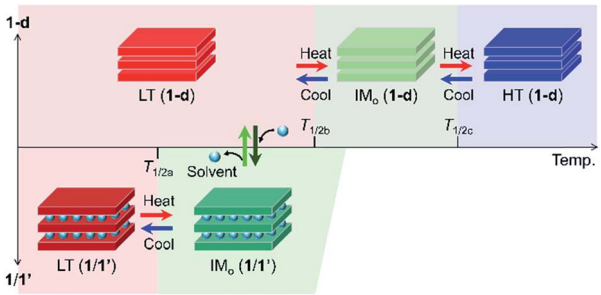

Scheme 2 Temperature-scale representation of the charge-ordered states in **1**/**1**′ and **1-d**, where the top and bottom scales are for **1-d** and **1**/**1**′, respectively.

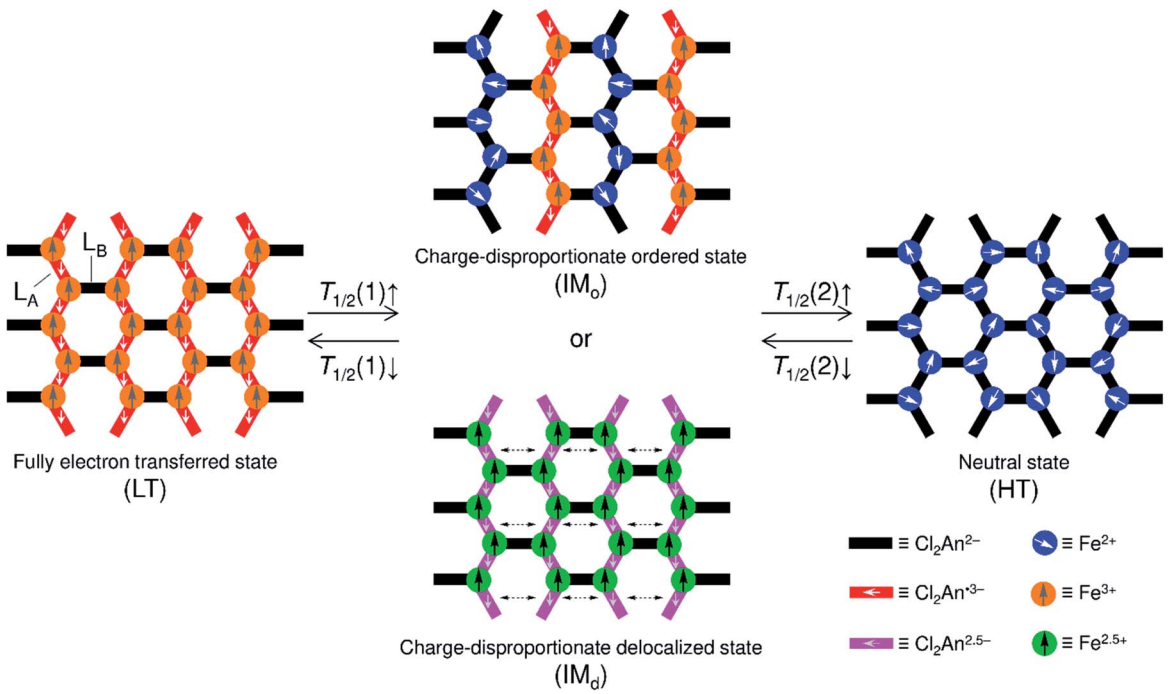

Scheme 1 Schematic illustrations of the variations of charge-ordered states in **1** and **1-d**, where the fully electron transferred state, charge-disproportionate ordered state, charge-disproportionate delocalized state, and neutral state are represented as LT, IM_o, IM_d, and HT phases, respectively.

crystal. These TDETs consequently revealed five material states with three unique charge-ordered states (LT, IM_o, and HT) that are formable in a D_2A_3 honeycomb-layered system. This type of TDET material has good potential for use as a stimuli-controllable molecular multi-switch.

Results and discussion

Preparation of 1-d and its structural overview

The pristine solvated compound, $(NPr_4)_2[Fe_2(Cl_2An)_3]\cdot 2(acetone)\cdot H_2O$ (**1**), which is prepared in accordance with a previously reported method,[31] has a flat honeycomb anionic layer $[Fe_2(Cl_2An)_3]^{2-}$ that is separated by two kinds of structurally distinguished NPr_4^+ cations (C_1^+ and C_2^+), forming an alternating stacking form $[\cdots(l)(C_1^+)(l)(C_2^+)\cdots]_\infty$ (l means the $[Fe_2(Cl_2An)_3]^{2-}$ layer) with position-disordered water molecules located only at one side of cation layers and two acetone molecules located inside the hexagonal pores of the $[Fe_2(Cl_2An)_3]^{2-}$ layer.[31]

The lattice solvent molecules in **1** can be easily removed by evacuating at room temperature for several hours to produce the desolvated compound, $(NPr_4)_2[Fe_2(Cl_2An)_3]$ (**1-d**), with its crystallinity remaining intact (here, it took 12 h to complete the elimination). Thermal gravimetric analysis (TGA) shows that the elimination of lattice solvents is completed by heating up to ~340 K under N_2 atmosphere conditions, and the compound of **1-d** is very stable up to *ca.* 500 K (Fig. S1†). The crystallinity of **1-d** was confirmed by performing single-crystal and powder X-ray diffraction (SC- and P-XRD) studies (Fig. 2 and S2;† *vide infra*). However, with the exposure of the crystalline sample of **1-d** to a vapor of a 1 : 2 v/v mixture of water/acetone at room temperature for 2–3 h, the solvated form, namely **1**, was recovered (as **1′**) with the pristine structure (Fig. S3, S4 and Table S1†). TGA of **1′** proves the contamination of the same amount of lattice solvents, *i.e.*, 2(acetone)·H_2O, and follows the same profile as that found for **1** (Fig. S1†).

SC-XRD analysis of **1-d** was first performed at 103 K, which revealed a 2D honeycomb-layered structure that is similar to that of **1**. While **1** was crystallized in the monoclinic space group $P2_1/c$ ($Z = 4$),[31] **1-d** crystalized in the space group of $P2_1/n$ with $Z = 2$, which determined a half of the formula unit to be an asymmetric unit ($1 \times Fe^{n+}$, $1.5 \times Cl_2An^{m-}$ ($L_A \times 1$, $L_B \times 0.5$), and $1 \times NPr_4^+$; Fig. 2a and Table S2†) with two-fold axes through the Fe^{n+} and the midpoint of the L_B Cl_2An^{m-} ligand. The Fe^{n+} node has a distorted octahedral Δ or Λ coordination geometry with three bidentate O atoms from two L_A ligands and one L_B bridging ligand, forming an anionic hexagonal layer $[Fe_2(Cl_2An)_3]^{2-}$ spreading parallel to the (10−1) plane (Fig. 2b), where the Δ and Λ geometric coordinations on the Fe^{n+} nodes are present alternately. The NPr_4^+ cations are located between the $[Fe_2(Cl_2An)_3]^{2-}$ layers, separating the layers with an interlayer distance of 8.817 Å (Fig. 2c). Thus, remarkable structural differences between the solvated (**1** and **1′**) and the desolvated (**1-d**) compounds are found in the structural symmetry of the formula unit and in the interlayer space shortened in **1-d** (Fig. 2). It should be noted that the NPr_4^+ cations are evenly located between the $[Fe_2(Cl_2An)_3]^{2-}$ layers in **1-d**, influencing

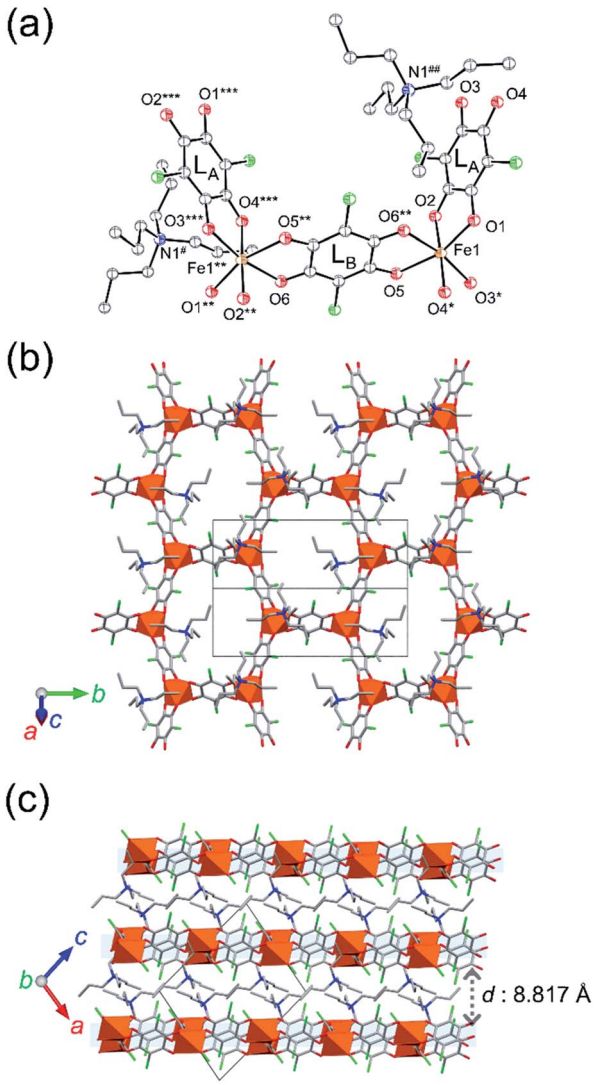

Fig. 2 Crystal structure of **1-d** at 103 K. (a) Structure of the formula unit (50% probability ellipsoids; symmetry operation (*) 1/2 + *x*, 3/2 − *y*, 1/2 + *z*; (**) −*x*, 1 − *y*, 1 − *z*; (***) −1/2 − *x*, −1/2 + *y*, 1/2 − *z*; (#) 1/2 − *x*, −1/2 + *y*, 1/2 − *z*; (##) −1 + *x*, *y*, *z*). (b) Projection of hexagonal honeycomb networks along the ⟨10−1⟩ direction, where Fe, C, N, O, and Cl atoms are colored in orange octahedra, gray, blue, red, and green, respectively, and hydrogen atoms are omitted for clarity. (c) Projection of layer structures along the *b*-axis, where the colors of atoms are the same as those in (b) and hydrogen atoms are omitted for clarity.

equal electrostatic effects for all Fe^{n+} nodes and the L_A Cl_2An^{m-} ligands, whereas the presence of two structurally characterized NPr_4^+ cations in **1** distinguishes the electrostatic effect for the Fe^{n+} sites and the L_A Cl_2An^{m-} ligands.

This electrostatic situation could significantly affect the stabilization of the electronic states of **1-d** and **1** (*vide infra*).

To determine the oxidation state of the Fe^{n+} node and the Cl_2An^{m-} ligand, it is convenient to verify the local bond lengths of Fe–O and C–O in the Cl_2An^{m-} ligands because of their sensitivity to the oxidation states; a comparison of the mean bond lengths d_{av}(Fe–O) for each octahedral Fe^{n+} node and

d_{av}(C–O) for each Cl_2An^{m-} ligand is made. In general, d_{av}(C–O) is found to be within the range of 1.244–1.270 Å and 1.289–1.312 Å for Cl_2An^{2-} and $Cl_2An^{\bullet 3-}$, respectively.[30,31] The d_{av}(C–O) value at 103 K for **1-d** was 1.293(3) Å and 1.257(3) Å for L_A and L_B, respectively, which are assigned the oxidation states of $Cl_2An^{\bullet 3-}$ and Cl_2An^{2-}, respectively. On the other hand, the d_{av}(Fe–O) value tends to be within the range of 2.091–2.140 Å and 2.000–2.050 Å for high-spin Fe^{2+} and Fe^{3+}, respectively.[30,31] The d_{av}(Fe–O) value at 103 K for **1-d** was 2.019(2) Å, which indicates the presence of the high-spin Fe^{3+} state. These situations imply that the charge-ordered state of **1-d** at 103 K is in the LT state with the formula of $[(Fe^{3+})_2(Cl_2An^{2-})(Cl_2An^{\bullet 3-})_2]^{2-}$, where the $Cl_2An^{\bullet 3-}$ bridging ligands are L_A, which makes a quasi-chain with Fe^{3+} along the [101] direction, and the Cl_2An^{2-} L_B bridging ligand links these chains alternately (along the [010] direction) to form the hexagonal net. Although the LT state in **1** underwent a transition at $T_{1/2a}$ = 237 K,[31] the LT state of **1-d** is stabilized even at 300 K without there being significant changes in bond lengths (Fig. S5 and Table S3†). Thus, the desolvation treatment of **1** at room temperature (300 K), changing to **1-d**, successfully demonstrated a change in the charge-ordered state involving an electron transfer: the IM_o phase $[(Fe^{2+})(Fe^{3+})(Cl_2An^{2-})_2(Cl_2An^{\bullet 3-})]^{2-}$ in **1** → the LT phase $[(Fe^{3+})_2(Cl_2An^{2-})(Cl_2An^{\bullet 3-})_2]^{2-}$ in **1-d**. It should be noted that this sponge behavior is reversible *via* the solvation procedure to form **1** (=**1′**) (Fig. S6†).

Magnetic characterization for the LT phase in 1-d

The magnetization (M_m) measurements for **1-d** were first performed over the temperature range of 1.8–300 K under an applied magnetic field of H_{dc} = 1 kOe. The temperature dependence of the magnetic susceptibility ($\chi_m = M_m/H_{dc}$) of **1-d** in this temperature region is similar to that observed for the LT phase in **1** (Fig. 3),[31] in that it can be described as a ferrimagnetic chain of S = 5/2 for Fe^{3+} and S = 1/2 for the L_A $Cl_2An^{\bullet 3-}$ ligand, which are weakly perturbed by interchain antiferromagnetic interactions through the L_B Cl_2An^{2-} bridge and interlayer through space.

The $\chi_m T$ value at 300 K is 13.3 cm^3 K mol^{-1}, which is slightly greater than the theoretical value (9.5 cm^3 K mol^{-1}) for a sum of magnetically isolated species of $Cl_2An^{\bullet 3-}$ (S = 1/2, g = 2.0) and high-spin Fe^{3+} (S = 5/2, g = 2.0). This is indicative of strongly coupled spins, even at 300 K (*vide infra*).[40–42] Upon decreasing the temperature, χ_m gradually increased and reached a maximum of 2.08 cm^3 mol^{-1} at 23 K, followed by an abrupt decrease to 1.45 cm^3 mol^{-1} at 1.8 K. The χ_m–T plot in the temperature range of 35–300 K was simulated by using the Seiden model with alternating S = 5/2 and S = 1/2 spins, including a mean-field approximation (zJ') to consider interchain interactions.[43] The fitting of the data for **1-d** provided an adequate parameter set of $g_{Fe} = g_L$ = 2.0 (fixed), J = −125.2 cm^{-1}, and zJ' = −0.27 cm^{-1}, which are comparable to those of **1** (J = −130.6 cm^{-1} and zJ' = −0.27 cm^{-1}) (Fig. 3).[31]

Field-cooled magnetization (FCM) curves obtained with several dc fields showed an elimination of the χ_m peak at T_{ex} with increasing applied external dc field, which is indicative of spin flipping behavior from an antiferromagnetic (AF) ground state (Fig. S7a†). In addition, the field dependence of the magnetization (M–H) measured at low temperatures revealed sigmoidal features with spin-flipping fields (H_{ex}, which was determined from a peak in dM/dH data at each temperature measured) as well as a small field hysteresis with H_c = 0.14 T at 1.8 K (Fig. S7b†). This is a typical case of metamagnetic behavior in low-dimensional magnetic systems; the inset of Fig. 3 displays an H/T phase diagram made from H_{ex} and T_{ex}, which separates the regions of paramagnetic (P) and AF phases.

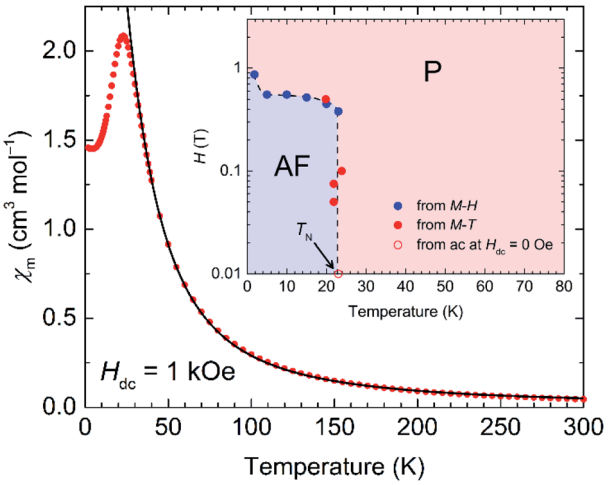

Fig. 3 Field-cooled χ_m ($\chi_m = M_m/H_{dc}$) for **1-d** measured with a dc field (H_{dc}) of 1 kOe for a temperature range of 1.8 K to 300 K, where the black solid line represents the best-fit line with the Seiden model using alternating classical S = 5/2 and quantum S = 1/2 spins for the data between 35 and 300 K (see the text). Inset: H/T phase diagram for **1-d**, where AF and P represent the antiferromagnetic and paramagnetic phases, respectively, where T_N (23 K) was determined from the χ' *versus* T data at H_{dc} = 0, and the black dashed line is a guide for enhanced visibility.

To investigate in more detail the magnetic behavior, the temperature dependence of the ac susceptibilities was measured at several frequencies below 60 K by applying an oscillating magnetic field (H_{ac} = 3 Oe) and a dc field of H_{dc} = 0 Oe. The in-phase susceptibility (χ') showed three kinds of peaks at around 23 K (broad), 20 K, and 5 K (Fig. S8a†), where the frequency-independent peaks at 23 K do not involve any anomaly of out-of-phase susceptibility (χ''), which is indicative of the occurrence of an AF phase transition with T_N = 23 K following the phase diagram (inset of Fig. 3). The other peaks at around 20 K and 5 K are slightly frequency dependent and involve an anomaly of χ'', albeit weak. Although a similar ac susceptibility feature was observed in **1**, which revealed single-chain magnet (SCM) behavior,[31] this behavior in **1-d** ruled out the possibility of SCM, and this may be due to a strong contribution of interchain antiferromagnetic interactions that possibly form some magnetic random domains in the AF phase. Actually, a fitting of the χ''–T curves using the Arrhenius law $\tau(T) = \tau_0 \exp(\Delta_\tau/k_BT)$ provided a much faster τ_0 value of 1.3 × 10^{-19} s with Δ_τ/k_B = 148.3 K; this is similar to a glassy behavior (Fig. S8b†).[44,45] Thus, the significant magnetic change from **1** to **1-d** could be attributed primarily to the structural contraction associated with the shorter interlayer distance in **1-d** (Fig. 2).

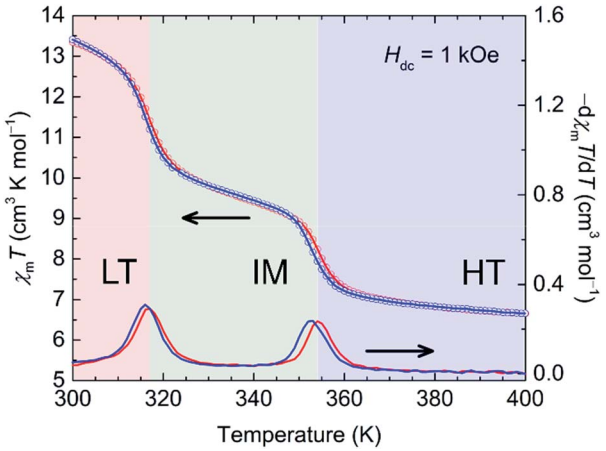

Fig. 4 Temperature dependence of $\chi_m T$ and $-d(\chi_m T)/dT$ for **1-d** measured at $H_{dc} = 1$ kOe continuously between 300 K and 400 K in initial heating (red) and post-cooling (blue) processes, where the LT, IM, and HT phases are displayed as red, green, and blue areas, respectively.

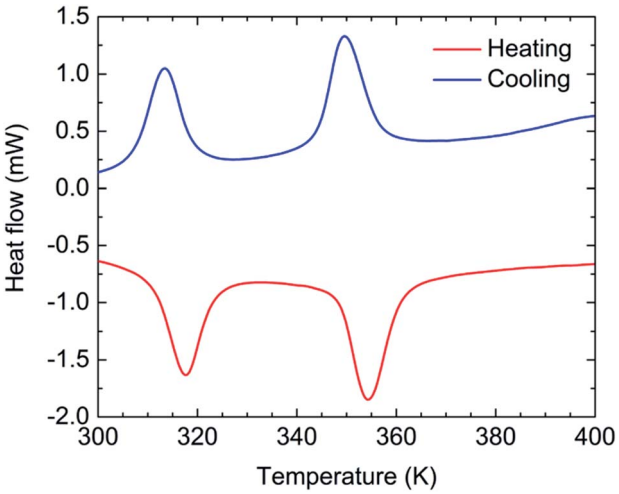

Fig. 5 Temperature dependence of the heat flow obtained from differential scanning calorimetry (DSC) values for **1-d** with a sweep rate of 5 K min^{-1}.

Thermally driven electron transfers in 1-d: from magnetic investigation

The temperature dependence of M_m of **1-d** was investigated for the HT region of 300–400 K. The M_m–T curve clearly shows two steps as the temperature is varied; Fig. 4 shows $\chi_m T$ variations as a function of temperature (χ_m *vs.* T in Fig. S9†). Upon heating from 300 K, the $\chi_m T$ value of 13.3 cm^3 K mol^{-1} at 300 K gradually decreases, but it decreases steeply at around $T_{1/2b}\uparrow = 317$ K and $T_{1/2c}\uparrow = 354$ K to 6.7 cm^3 K mol^{-1} at 400 K, indicating the occurrence of TDET from the LT phase to the HT phase *via* an IM phase. The $\chi_m T$ value at 400 K (HT phase) is close to the theoretical value of 7.3 cm^3 K mol^{-1} for the magnetically isolated species of $Fe^{2+}{}_{HS}$ ($S = 2$ as $g = 2.2$),[31] and the $\chi_m T$ value of 9.6 cm^3 K mol^{-1} at 335 K for the IM phase is almost half the value (10.0 cm^3 K mol^{-1}) between those of the HT and LT phases. The cooling process almost follows the feature of the heating process with little thermal hysteresis ($\Delta T_{1/2} = 1$ K), where $T_{1/2}$ was determined from peaks of $d\chi_m T/dT$ plots (Fig. 4). The stepwise TDET behavior of **1-d** was also confirmed by performing differential scanning calorimetry (DSC) measurements (Fig. 5).

SC-XRD study for the phases in 1-d

Because the crystals of **1-d** are stable at high temperatures, SC-XRD analyses at 335 K and 380 K, which correspond to the IM phase and the HT phase, respectively, were conducted as well as at 300 K for the LT phase in order to obtain a comparison under the same measurement conditions using the same apparatus (Fig. 6a, c, e and Table S4†). At all temperatures, they crystalized in monoclinic $P2_1/n$ with $Z = 2$ as well as at 103 K, and the crystal lattices are also similar to each other. Nevertheless, the local distances within these structures were characteristically varied.

The d_{av}(C–O) values for L_A and L_B and the d_{av}(Fe–O) value at 300 K are 1.286(6), 1.260(7), and 2.027(4) Å, respectively (Fig. 6a

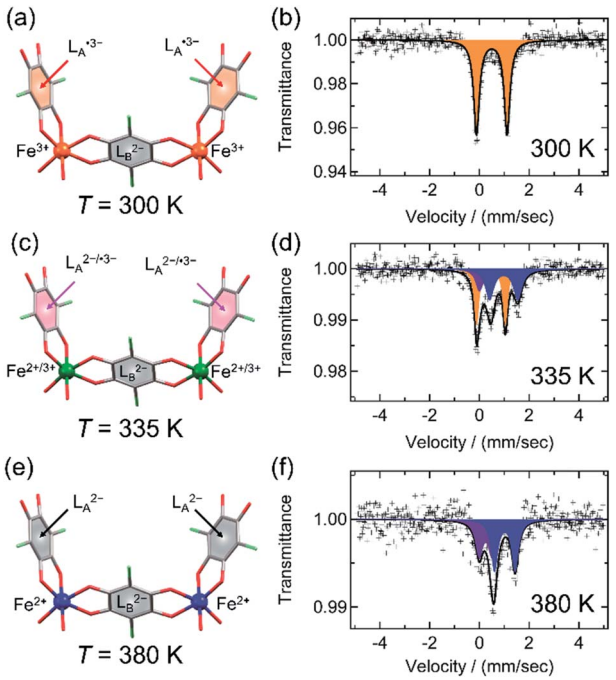

Fig. 6 Charge variations of the core unit and ^{57}Fe Mössbauer spectra of **1-d** in LT at 300 K (a and b), IM_o at 335 K (c and d), and HT at 380 K (e and f). (a, c, and e) Display of charge variations, where L^{2-}, $L^{2-/\bullet 3-}$, and $L^{\bullet 3-}$ are displayed as gray-, pink-, and red-filled C6 rings, respectively, and Fe^{2+}, Fe^{2+}/Fe^{3+}, and Fe^{3+} are displayed in blue, green, and orange, respectively, with C, O, and Cl atoms in gray, red, and green, respectively. (b, d, and f) ^{57}Fe Mössbauer spectra for the respective phases. The solid lines in the Mössbauer spectra are Lorentzian curves obtained using the parameters in Table S6,† where orange and blue curves correspond to high-spin Fe^{3+} and high-spin Fe^{2+} species, respectively. The purple curves observed at 330 K and 380 K, with similar parameters of δ and ΔE_Q may correspond to the impurity of decomposition species due to the higher temperature for longer measurement times, even in a nitrogen atmosphere.

and Table S5†), which are consistent with the LT charge-ordered state of $[(Fe^{3+})_2(Cl_2An^{2-})(Cl_2An^{\cdot 3-})_2]^{2-}$, as found at 103 K (*vide supra*). ^{57}Fe Mössbauer spectra recorded at 300 K show only a typical spectrum of $Fe^{3+}{}_{HS}$ (Fig. 6b and Table S6†).[30,31] However, at 335 K, only the d_{av}(C–O) value of L_A changes to be lower as 1.271(7) Å, which is just an intermediate between the cases of Cl_2An^{2-} and $Cl_2An^{\cdot 3-}$, while d_{av}(C–O) = 1.254(9) Å for L_B is still within the range of Cl_2An^{2-} (Fig. 6c and Table S5†). In addition, the d_{av}(Fe–O) value of 2.058(4) Å is also an intermediate between those of Fe^{2+}–O and Fe^{3+}–O (Table S5†). This bonding formation indicates that the phase at 335 K is in an IM phase, although a half of the structure was determined by this lab-level SC-XRD measurement. This IM state for **1-d** at 335 K could be assigned to be a positional disorder of the $[(Fe^{2+})(Fe^{3+})(Cl_2An^{2-})_2(Cl_2An^{\cdot 3-})]^{2-}$ state made in each layer that is similarly found in the IM phase in **1**.[31] This conclusion was also supported by SC-XRD measurements using a synchrotron (SPring-8, Hyogo) (ESI†). Meanwhile, ^{57}Fe Mössbauer spectroscopy performed at 335 K revealed that the $Fe^{2+}{}_{HS}$ and $Fe^{3+}{}_{HS}$ species were evenly located in the mode of IM_o (like in **1**), not in the mode of the charge-disproportionate delocalized state (IM_d) in Scheme 1, on the time scale of the Mössbauer effect ($t \approx 10^{-7}$ to 10^{-10} s) (Fig. 6d and Table S6†).[30,31,41] In the related system, fast electron exchange between mixed-valent Fe^{2+}/Fe^{3+} species has been proposed using Mössbauer studies.[42,46]

As the temperature was finally increased to 380 K, the d_{av}(C–O) value of L_A is further decreased to 1.252(8) Å, corresponding to a case of Cl_2An^{2-}, as well as L_B (d_{av}(C–O) = 1.26(1) Å) (Fig. 6e and Table S5†). Correspondingly, d_{av}(Fe–O) = 2.096(5) Å is within the range for Fe^{2+}–O (Table S5†). This feature satisfies the fact that the homovalent HT phase of $[(Fe^{2+}{}_{HS})_2(Cl_2An^{2-})_3]^{2-}$ was formed. Actually, the ^{57}Fe Mössbauer spectra recorded at 380 K agreed well with the existence of the high-spin Fe^{2+} state,[30,31] although some impurities that may have been produced by compound decomposition were isolated in HT measurements (Fig. 6f and Table S6†).[47] Thus, the structures measured at 335 K and 380 K prove what was observed in the temperature dependence of M_m, *i.e.*, two-step TDET behavior (*vide supra*).

The difference of $T_{1/2(1)}$ between **1** and **1-d**, where $T_{1/2(1)}\uparrow$ = 317 K in **1-d**, is much higher than $T_{1/2(1)}\uparrow$ = 237 K in **1**, and this could be associated with the effect of Coulomb interactions between the layers and NPr_4^+ cations, in particular, between the L_A $Cl_2An^{\cdot 3-}$ subunit and NPr_4^+. There are two kinds of $L_A\cdots NPr_4^+$ distances in **1**, *ca.* 4.9 Å and 6.2 Å,[31] where the shorter one could have a gain to be a higher valency of the $(Fe^{3+}–Cl_2An^{\cdot 3-})_\infty$ chain owing to electrostatic attraction; meanwhile, it may result in electrostatic repulsion to adjacent chains through the L_B Cl_2An^{2-} ligand. In addition to the fact that the other $L_A\cdots NPr_4^+$ distance (6.2 Å) is much longer than that, this situation in **1** could induce TDET between the LT and IM_o phases at a lower $T_{1/2(1)}$, at least relative to that in **1-d** (*vide infra*). Moreover, only one type of NPr_4^+ was assigned with the $L_A\cdots NPr_4^+$ distance of *ca.* 5.0 Å in **1-d**, which evenly load electrostatic interaction to the L_A ligand. This situation in **1-d** could stabilize the LT phase much more than that in **1**, so $T_{1/2(1)}$ in **1-d** > $T_{1/2(1)}$ in **1**.

In situ continuous modifications using desolvation/solvation treatments

These transition processes are accomplished in a single crystal even though it undergoes desolvation/solvation processes to convert between **1**/**1′** and **1-d**, which demonstrated the reversible magnetic variations in *ex situ* magnetic measurements (Fig. S10 and S11†). This means that we can address five states (LT and IM_o in **1**; LT, IM_o, and HT in **1-d**) comprising three identified phases of LT, IM_o, and HT phases (Scheme 2 and Fig. 7). To demonstrate the effects of these continuous variations of the phases on temperature control and guest molecule accommodation, *in situ* magnetic measurements for continuous changes between **1** and **1-d** were conducted using a SQUID apparatus (MPMS-XL, Quantum Design Co. Ltd.). The use of

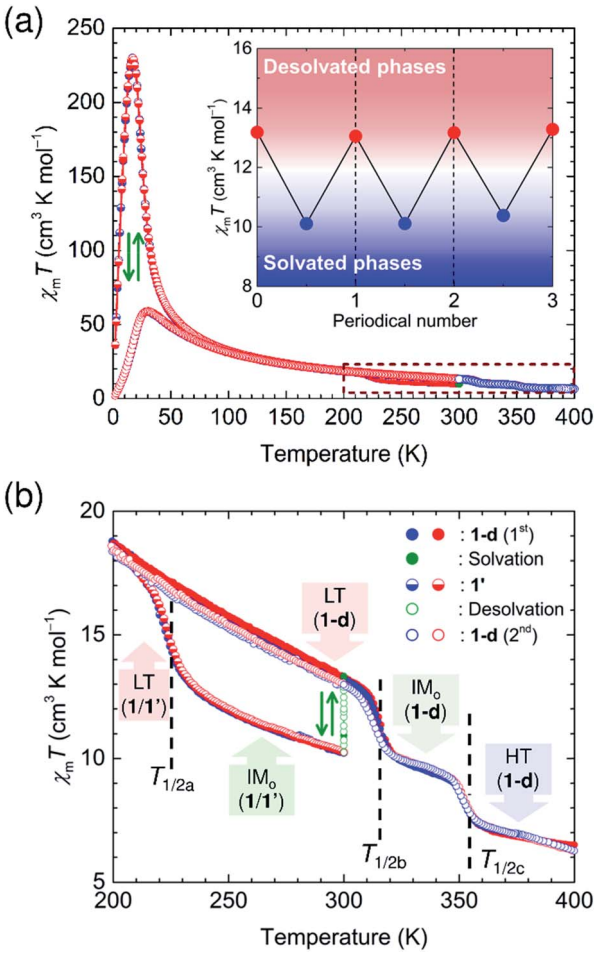

Fig. 7 *In situ* magnetic measurements ($\chi_m T$–T plots) performed at 1 kOe throughout the processes for **1** (**1′**) and **1-d** in a closed cell with a valve connectable to either a vapor of the solvent or TMP (solvation/desolvation was performed at 300 K). (a) Overview of $\chi_m T$–T plots in the temperature range of 1.8 K and 400 K, where the initial sweep of field-cooled magnetization was started from **1-d** prepared under *ex situ* conditions at 300 K followed by a coherent sweep of 300 K → 1.8 K → 300 K → 400 K → 300 K → exposed to a vapor of acetone–water mixed solution at 300 K → 1.8 K → 300 K → evacuating at 300 K → 1.8 K → 300 K → 400 K → 300 K. The inset shows a switching demonstration at 300 K by repeating the solvent vapor-insertion and the evacuation. (b) Close-up view of the part at 200–400 K.

a home-made closed cell enables the insertion of gaseous solvent molecules as well as evacuation at a turbomolecular pump (TMP) level.

First, a polycrystalline sample of **1-d** (the solvent-free compound) was put into the SQUID apparatus at 300 K. Then, a temperature sweep of 300 K → 1.8 K → 300 K was applied for **1-d** (Fig. 7a). During this process, the absence of TDET behavior was confirmed in this temperature region, corresponding to the magnetic data for the LT phase of **1-d**. As the temperature increased to 400 K, stepwise charge variations from LT (**1-d**) to IM_o (**1-d**) at $T_{1/2b}\uparrow$ and from IM_o (**1-d**) to HT (**1-d**) at $T_{1/2c}\uparrow$ were observed (Fig. 7b). During the cooling process from 400 K to 300 K, the charge variation followed the heating process for **1-d** as HT (**1-d**) → IM_o (**1-d**) → LT (**1-d**) at $T_{1/2c}\downarrow$ and $T_{1/2b}\downarrow$, respectively (Fig. 7b). At 300 K, the sample was exposed to solution vapor of a 1 : 2 v/v mixture of water/acetone, for which the $\chi_m T$ value was monitored in a time course, showing a rapid decrease from 13.3 cm^3 K mol^{-1} for LT (**1-d**) into a saturation with 10.1 cm^3 K mol^{-1} for the IM phase of **1**, *i.e.*, **1′** within a few minutes (Fig. 7b and S12a†). Upon cooling to 1.8 K, the TDET for the transformation from IM_o into LT in **1′** occurred at $T_{1/2a}\downarrow$, which was followed by TDET from LT to IM_o at $T_{1/2a}\uparrow$ during the heating process up to 300 K (Fig. 7b). After this process, the sample of **1′** was kept standing at 300 K for 12 h with an adequate evacuation, for which the $\chi_m T$ value was monitored in a time course, showing a gradual increase from 10.2 cm^3 K mol^{-1} for the IM_o phase of **1′** followed by a saturation with 13.1 cm^3 K mol^{-1} for the LT phase of **1-d** owing to the desolvation process (Fig. 7b and S12b†). This reversible charge modulation of **1**/**1-d** was confirmed by performing the solvation/desolvation process at 300 K over several cycles (inset of Fig. 7a and S12†). Consequently, this course of processes proves that the respective TDET processes of **1′** and **1-d** can be combined using the desolvation/solvation processes at around room temperature for the same sample of compounds (Fig. 7 and S12†).

Furthermore, *in situ* magnetic measurements from **1** to **1-d** were conducted in the heating process from 300 to 400 K at a rate of 0.5 K min^{-1} in a sweep mode (Fig. S13†). The desolvation of crystallization solvent from **1** spontaneously occurred as the temperature was increased up to ~320 K, and resulted in the gradual variations of $\chi_m T$ values associated with the material state changes from IM_o (**1**) to IM_o (**1-d**).

Electronic conductivity of 1-d

The charge variations in **1-d** associated with TDET behavior resulted in characteristic temperature-dependent electronic conductivity. The electronic conductivity measurements were performed on a hexagonal-shaped single crystal of **1-d** using two-probe dc current–voltage techniques in heating/cooling processes with a sweep rate of 5 K min^{-1} (Fig. 8a). Gold wire probes were attached (i) parallel (||) and (ii) perpendicular ($\perp_c$) to the Fe–L_A chain direction, and (iii) perpendicular ($\perp_l$) to the layer direction (Fig. S14†), respectively. Note that the (i) arrangement corresponds to the direction experiencing TDET behavior. As expected, the room temperature conductivity parallel to the layers $\sigma_{\parallel}$ and $\sigma_{\perp_c}$ (*ca.* 2.6 × 10^{-4} S cm^{-1} and *ca.*

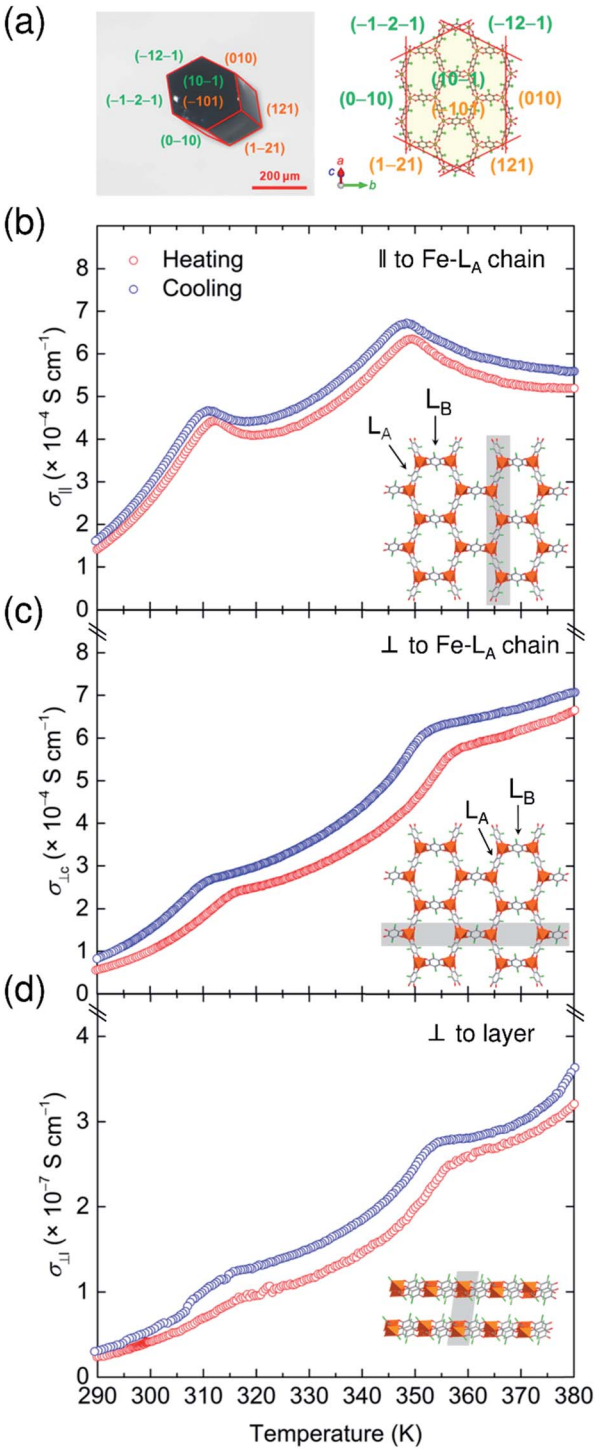

Fig. 8 Thermal variation of single-crystal electronic conductivity for **1-d** using a typical size of hexagonal crystals (a), in which gold wire probes were attached parallel (||; b) and perpendicular ($\perp_c$; c) to the Fe–L_A chains in the layer, and perpendicular to the layer-stacked direction ($\perp_l$; d).

1.0 × 10^{-4} S cm^{-1}, Fig. 8b and c) is much higher than that perpendicular to the hexagonal layers ($\sigma_{\perp_l}$, *ca.* 4.1 × 10^{-8} S cm^{-1}; Fig. 8d), resulting in a significant anisotropic electronic conductivity ($\sigma_{\parallel}/\sigma_{\perp_l}$ = *ca.* 6.3 × 10^3).[42,48] The observed electronic

conductivity in **1-d** at room temperature was comparable with that in previously reported honeycomb layers.[41,49]

During the heating process, the thermal variations of $\sigma_{\parallel}$ profiles showed an unusual incoherent feature with two-step inflections at around $T_{1/2b}$ and $T_{1/2c}$ (Fig. 8b). The cooling process also follows the features of the heating process. The absolute value of σ is still within the range for common semiconductors, but interestingly, the HT phase region (350–380 K) of $\sigma_{\parallel}$ showed metallic behavior, and even in the IM_o phase region (310–350 K), such a metallic feature was observed at higher temperatures of $T_{1/2b}$ and $T_{1/2c}$. This behavior may be due to electronic fluctuations that are closely associated with TDET at $T_{1/2b}$ and $T_{1/2c}$. A similar feature was previously reported in DA systems involving TDET (*i.e.*, N–I transition systems).[18,50] The activation energy (E_a) for the semiconductor behavior in the LT phase and the IM_o phase during the heating process is 438.4 meV (285–310 K) and 189.9 meV (328–347 K), respectively (Fig. S15†). The decreasing tendency of E_a values associated with the phase transition from LT to HT *via* IM_o phases indicates that the electronic band structure was modified in each phase based on the occurrence of TDET. The inflections at around $T_{1/2}$s were significant for $\sigma_{\parallel}$; however, the thermal variation of the $\sigma_{\perp_c}$ and $\sigma_{\perp_l}$ values exhibited fewer features owing to the anisotropic environment of TDET behavior (Fig. 8c and d).

Conclusions

There are few stimuli responsive molecular materials that can multiply change their charge states. In addition, there are no cases in which two types of phase-switchable materials, each of which has its own TDET process, were combined with each other using a guest-induced ET process. The present material is the first case of such materials. The transformation between these accessible five states composed of three distinct charge-ordered states (LT, IM_o, and HT) was successfully realized using two kinds of stimuli, namely temperature control and guest molecule desorption/adsorption. These stepwise TDETs in **1-d** resulted in electronic fluctuations, which had anisotropic transient electronic conductivity; the Fe–L_A chain direction, *i.e.*, corresponding to the TDET direction, is more conductive than the other directions.

Even though the basic layer frameworks of **1** and **1-d** are structurally very similar to each other, $T_{1/2a}$ and $T_{1/2b}$ for the LT $\rightleftharpoons$ IM_o TDET in **1** and **1-d**, respectively, are largely different, which could be attributed to the differences in the electrostatic effects in **1** and **1-d**, which resulted from their packing arrangement of NPr_4^+ cations. Thus, the desolvation/solvation process between **1** and **1-d** caused a structural change. In particular, the packing arrangement of the anionic $[Fe_2(Cl_2An)_3]^{2-}$ layer and the cations NPr_4^+ contributed significantly to modulating the electrostatic effect in the TDET of this series. This conclusion may answer the question regarding the reason why other series of $(C)_2[Fe_2(Cl_2An)_3]$ with different C^+ cations reported so far did not exhibit such TDETs within the common temperature range. The bulk effect brought about by electrostatic stabilization, *i.e.*, Madelung stabilization, is very important to the tuning of TDET in ionic D/A systems.

Conflicts of interest

There are no conflicts to declare.

Acknowledgements

The authors thank Prof. S. Hayami (Kumamoto University) for the helpful discussions on ^{57}Fe Mössbauer spectra and Dr K. Sugimoto (JASRI) for the SC-XRD measurements for the IM phase using a synchrotron beam at Spring-8. This work was supported by a Grant-in-Aid for Scientific Research (No. 16H02269, 18K19050, 18K05055, and 18H05208) from MEXT, Japan, and on Innovative Areas ("π-System Figuration" Area 2601, No. 17H05137) from the Japan Society for the Promotion of Science (JSPS), Japan, and the E-IMR project. Y. S. is thankful for financial support received from the TOBE MAKI Scholarship Foundation and the Shorai Foundation for Science and Technology. J. C. gratefully acknowledges the financial support received from the Chinese Scholarship Council (CSC) and the Institute for Materials Research, Tohoku University.

Notes and references

1 A. Dei, D. Gatteschi, C. Sangregorio and L. Sorace, *Acc. Chem. Res.*, 2004, **37**, 827–835.
2 O. Sato, *Nat. Chem.*, 2016, **8**, 644–656.
3 M. E. Guillermo and E. Coronado, *Chem. Soc. Rev.*, 2018, **47**, 533–557.
4 R. M. Buchanan and C. G. Pierpont, *J. Am. Chem. Soc.*, 1980, **102**, 4951–4957.
5 J. B. Torrance, A. Girlando, J. J. Mayerle, J. I. Crowley, V. Y. Lee and P. Batail, *Phys. Rev. Lett.*, 1981, **47**, 1747–1750.
6 A. Caneschi, A. Dei, F. F. de Biani, P. Gütlich, V. Ksenofontov, G. Levchenko, A. Hoefer and F. Renz, *Chem.–Eur. J.*, 2001, **7**, 3926–3930.
7 T. Nakamoto, Y. Miyazaki, M. Itoi, Y. Ono, N. Kojima and M. Sorai, *Angew. Chem., Int. Ed.*, 2001, **40**, 4716–4719.
8 M. Mitsumi, K. Kitamura, A. Morinaga, Y. Ozawa, M. Kobayashi, K. Toriumi, Y. Iso, H. Kitagawa and T. Mitani, *Angew. Chem., Int. Ed.*, 2002, **41**, 2767–2771.
9 S. Horiuchi, R. Kumai, Y. Okimoto and Y. Tokura, *Chem. Phys.*, 2006, **325**, 78–91.
10 N. G. R. Hearns, J. L. Korcok, M. M. Paquette and K. E. Preuss, *Inorg. Chem.*, 2006, **45**, 8817–8819.
11 D. Kiriya, H. C. Chang and S. Kitagawa, *J. Am. Chem. Soc.*, 2008, **130**, 5515–5522.
12 D. F. Li, R. Clérac, O. Roubeau, E. Harté, C. Mathonière, R. L. Bris and S. M. Holmes, *J. Am. Chem. Soc.*, 2008, **130**, 252–258.
13 S. Takaishi, M. Takamura, T. Kajiwara, H. Miyasaka, M. Yamashita, M. Lwata, H. Matsuzaki, H. Okamoto, H. Tanaka, S. Kuroda, H. Nishikawa, H. Oshio, K. Kato and M. Takata, *J. Am. Chem. Soc.*, 2008, **130**, 12080–12084.

14 T. Liu, Y. J. Zhang, S. Kanegawa and O. Sato, *J. Am. Chem. Soc.*, 2010, **132**, 8250–8251.
15 M. Nihei, Y. Sekine, N. Suganami and H. Oshio, *Chem. Lett.*, 2010, **39**, 978–979.
16 M. Nihei, Y. Sekine, N. Suganami, K. Nakazawa, A. Nakano, H. Nakano, Y. Murakami and H. Oshio, *J. Am. Chem. Soc.*, 2011, **133**, 3592–3600.
17 P. Dapporto, A. Dei, G. Poneti and L. Sorace, *Chem.–Eur. J.*, 2008, **14**, 10915–10918.
18 H. Miyasaka, N. Motokawa, T. Chiyo, M. Takemura, M. Yamashita, H. Sagayama and T. Arima, *J. Am. Chem. Soc.*, 2011, **133**, 5338–5345.
19 N. Hoshino, F. Iijima, G. N. Newton, N. Yoshida, T. Shiga, H. Nojiri, A. Nakao, R. Kumai, Y. Murakami and H. Oshio, *Nat. Chem.*, 2012, **4**, 921–926.
20 M. Nihei, Y. Okamoto, Y. Sekine, N. Hoshino, T. Shiga, I. P. C. Liu and H. Oshio, *Angew. Chem., Int. Ed.*, 2012, **51**, 6361–6364.
21 K. G. Alley, G. Poneti, J. B. Aitken, R. K. Hocking, B. Moubaraki, K. S. Murray, B. F. Abrahams, H. H. Harris, L. Sorace and C. Boskovic, *Inorg. Chem.*, 2012, **51**, 3944–3946.
22 K. G. Alley, G. Poneti, P. S. D. Robinson, A. Nafady, B. Moubaraki, J. B. Aitken, S. C. Drew, C. Ritchie, B. F. Abrahams, R. K. Hocking, K. S. Murray, A. M. Bond, H. H. Harris, L. Sorace and C. Boskovic, *J. Am. Chem. Soc.*, 2013, **135**, 8304–8323.
23 Y. Z. Zhang, P. Ferko, D. Siretanu, R. Ababei, N. P. Rath, M. J. Shaw, R. Clérac, C. Mathonière and S. M. Holmes, *J. Am. Chem. Soc.*, 2014, **136**, 16854–16864.
24 M. Mitsumi, T. Nishitani, S. Yamasaki, N. Shimada, Y. Komatsu, K. Toriumi, Y. Kitagawa, M. Okumura, Y. Miyazaki, N. Córska, A. Inaba, A. Kanda and N. Hanasaki, *J. Am. Chem. Soc.*, 2014, **136**, 7026–7037.
25 K. Nakabayashi and H. Miyasaka, *Chem.–Eur. J.*, 2014, **20**, 5121–5131.
26 R. J. Wei, R. Nakahara, J. M. Cameron, G. N. Newton, T. Shiga, H. Sagayama, R. Kumai, Y. Murakami and H. Oshio, *Dalton Trans.*, 2016, **45**, 17104–17107.
27 K. Nakabayashi, M. Nishio and H. Miyasaka, *Inorg. Chem.*, 2016, **55**, 2473–2480.
28 O. Drath, R. W. Gable, B. Moubaraki, K. S. Murray, G. Poneti, L. Sorace and C. Boskovic, *Inorg. Chem.*, 2016, **55**, 4141–4151.
29 M. Nihei, Y. Yanai, I. J. Hsu, Y. Sekine and H. Oshio, *Angew. Chem., Int. Ed.*, 2017, **56**, 591–594.
30 J. A. DeGayner, K. Y. Wang and T. D. Harris, *J. Am. Chem. Soc.*, 2018, **140**, 6550–6553.
31 J. Chen, Y. Sekine, Y. Komatsumaru, S. Hayami and H. Miyasaka, *Angew. Chem., Int. Ed.*, 2018, **57**, 12043–12047.
32 O. Sato, T. Iyoda, A. Fujishima and K. Hashimoto, *Science*, 1996, **272**, 704–705.
33 S. Ohkoshi and H. Tokoro, *Acc. Chem. Res.*, 2012, **45**, 1749–1758.
34 A. Mondal, Y. L. Li, M. Seuleiman, M. Julve, L. Toupet, M. Buron-Le Cointe and R. Lescouëzec, *J. Am. Chem. Soc.*, 2013, **135**, 1653–1656.
35 Y. Sekine, M. Nihei, R. Kumai, H. Kakao, Y. Murakami and H. Oshio, *Inorg. Chem. Front.*, 2014, **1**, 540–543.
36 L. Egan, K. Kamenev, D. Papanikolaou, Y. Takabayashi and S. Margadonna, *J. Am. Chem. Soc.*, 2006, **128**, 6034–6035.
37 J. Zhang, W. Kosaka, K. Sugimoto and H. Miyasaka, *J. Am. Chem. Soc.*, 2018, **140**, 5644–5652.
38 W. Kosaka, Y. Takahashi, M. Nishio, K. Narushima, H. Fukunaga and H. Miyasaka, *Adv. Sci.*, 2018, **5**, 1700526.
39 J. Zhang, W. Kosaka, Y. Kitagawa and H. Miyasaka, *Angew. Chem., Int. Ed.*, 2019, **58**, 7351–7356.
40 I. R. Jeon, B. Negru, R. P. Van Duyne and T. D. Harris, *J. Am. Chem. Soc.*, 2015, **137**, 15699–15702.
41 J. A. DeGayner, I. R. Jeon, L. Sun, M. Dincă and T. D. Harris, *J. Am. Chem. Soc.*, 2017, **139**, 4175–4184.
42 S. A. Sahadevan, A. Abhervé, N. Monni, C. Sáenz de Pipaón, J. R. Galán-Mascarós, J. C. Waerenborgh, B. J. C. Vieira, P. Auban-Senzier, S. Pillet, E. E. Bendeif, P. Alemany, E. Canadell, M. L. Mercuri and N. Avarvari, *J. Am. Chem. Soc.*, 2018, **140**, 12611–12621.
43 J. Seiden, *J. Phys., Lett.*, 1983, **44**, 947–952.
44 D. F. Li, L. M. Zheng, Y. Z. Zhang, J. Huang, S. Gao and W. X. Tang, *Inorg. Chem.*, 2003, **42**, 6123–6129.
45 M. X. Yao, Q. Zheng, X. M. Cai, Y. Z. Li, Y. Song and J. L. Zuo, *Inorg. Chem.*, 2012, **51**, 2140–2149.
46 N. S. Ovanesyan, Z. K. Nikitina and V. D. Makhaev, *Bull. Russ. Acad. Sci.: Phys.*, 2017, **81**, 855–859.
47 M. M. Khusniyarov, T. Weyhermüller, E. Bill and K. Wieghardt, *Angew. Chem., Int. Ed.*, 2008, **47**, 1228–1231.
48 S. Benmansour, A. Abhervé, P. Gómez-Claramunt, C. Vallés-García and C. J. Gómez-García, *ACS Appl. Mater. Interfaces*, 2017, **9**, 26210–26218.
49 R. Murase, B. F. Abrahams, D. M. D'Alessandro, C. G. Davies, T. A. Hudson, G. N. L. Jameson, B. Boubaraki, K. S. Murray, R. Robson and A. L. Sutton, *Inorg. Chem.*, 2017, **56**, 9025–9035.
50 H. Miyasaka, T. Morita and M. Yamashita, *Chem. Commun.*, 2011, **47**, 271–273.

